Smart Structures and Systems, *Vol. 27, No. 5 (2021) 761-768*
DOI: https://doi.org/10.12989/sss.2021.27.5.761

Evaluation of crack opening phenomenon using subset-optimized digital image correlation

Myung Soo Kang [1], Seok Been Im [2] and Yun-Kyu An*[1]

[1] *Department of Architectural Engineering, Sejong University, 209 Neungdong-ro, Gwangjin-gu, Seoul, Republic of Korea*
[2] *Research Institute for Infrastructure Performance, KISTEC, 24 Ena-ro, 128beon-gil, Jinju-si, Gyeongsangnam-do, Republic of Korea*

(*Received May 14, 2020, Revised December 31, 2020, Accepted January 4, 2021*)

Abstract. This paper presents crack opening phenomenon evaluation using digital image correlation (DIC) with a statistically optimized subset size. In conventional DIC analysis, the subset sizes varying from several pixels to more than hundred pixels have been often selected by experts' subjective judgement based on conventional subset size determination algorithms. Since these conventional subset size determination algorithms, however, calculate speckle pattern features at a certain location of a single target image, it is difficult to consider not only all speckle pattern features within region of interest (ROI) but also the random measurement noises during the digital image acquisition process. To overcome the technical limitation, a statistical optimization algorithm of the subset size, which calculates the optimal subset size by the 3-loop iteration of normalized cross correlation within the entire ROI, is newly proposed. In addition, the optimal subset-based DIC analysis is applied to crack opening phenomenon evaluation in a mock-up concrete specimen under step loading conditions. The validation test results show 3.6 μm maximum error compared with the ground truth which is obtained by direct measurement, while a conventional subset size determination algorithm-based DIC analysis produces the maximum error of 62.7 μm.

Keywords: digital image correlation; optimal subset size; automated subset size determination; crack opening evaluation; statistical optimization

1. Introduction

A crack is one of the typical and critical damage types in structures. Once the crack occurs in structures, it may propagate along the structural surface and through-the-thickness directions by repeated external loads, resulting in degradation of structural integrity and safety. To effectively detect and evaluate the crack, a number of researchers have proposed various nondestructive evaluation (NDE) techniques such as ultrasonic (An *et al*. 2013, 2015, Kim *et al*. 2018), radio-frequency identification (Pour-Ghaz *et al*. 2014, Caizzone and DiGiampaolo 2015, Marindra and Tian 2018), microwave (Qaddoumi *et al*. 2000, Yun and Lim 2014), eddy current (Bohacova 2013, Camerini *et al*. 2018, Tsukamoto *et al*. 2018), thermography (Li *et al*. 2011, An *et al*. 2015, Jang and An 2018) and digital image correlation (DIC) (Hutt and Cawley 2009, Destrebecq *et al*. 2011, Ghorbani *et al*. 2014). Among these NDE techniques, DIC is a promising optical assessment tool for crack evaluation, because it enables to accurately measure surface deformation with a pixel unit in a fully noncontact way. Moreover, DIC is able to sequentially measure full-field responses with simple test setup and data acquisition procedure.

To effectively analyze the crack using DIC, users should carefully consider various analysis factors. For example, Sutton *et al*. (2018) investigated the effects of sub-pixel restoration on the measurement precision of DIC. Schreier and Sutton (2002) tested the systematic errors related to undermatched shape function. Sun and Pang (2007) pointed out that a subset size should have a lower limit in order to suppress the influence of random noises. Lecompte *et al*. (2006) studied the quality of the speckle patterns in terms of speckle spacing, speckle size and image resolution. Hua *et al*. (2011) investigated the effects of speckle size and density on DIC. Furthermore, correlation criterion (Tong 2005), measurement noise (Wang *et al*. 2007) and non-parallel charge-coupled device (Meng *et al*. 2006) issues have been widely studied.

In particular, the subset size is critical for DIC accuracy. The subset is basically defined as numerous small matrices which are divided from the target image matrix so that partial or small deformation within the target image can be analyzed. The smaller subset size could achieve higher DIC accuracy by increasing the spatial resolution. On the other hand, the insufficient subset size may not contain enough distinguishable speckle pattern features for the proper DIC analysis, meaning that there is a trade-off between the subset size and DIC accuracy. To address the trade-off issue, subset size determination algorithms have been proposed. For instance, Yaofeng and Pang (2007) suggested a subset entropy algorithm, which calculates the sum of absolute difference of eight neighboring points, for subset size selection. Then, Pan *et al*. (2008) proposed a sum of square of subset intensity gradient (SSSIG) algorithm, which evaluates local speckle pattern intensity using a

*Corresponding author, Ph.D., Professor,
E-mail: yunkyuan@sejong.ac.kr

ISSN: 1738-1584 (Print), 1738-1991 (Online)

threshold value of standard deviation (SD) error within a subset, for selecting a single subset size throughout the entire region of interest (ROI). However, these conventional algorithms assess only speckle pattern at a certain local area of a target image under the assumption of uniformly distributed speckle patterns within the entire ROI. Thus, spatially different DIC errors can be augmented when the speckle patterns are spatially biased on ROI of the target image. Furthermore, they highly depend on experts' subjective judgement or experience to determine the optimal threshold value for subset size determination. In this study, DIC analysis using a statistically optimized subset size, which automatically determines an optimal subset size by the 3-loop iteration of normalized cross correlation (NCC), is newly proposed. The proposed algorithm is able to minimize measurement and spatially different DIC errors by statistically optimizing the subset size within the entire ROI. Then, the proposed algorithm is experimentally validated through crack opening phenomenon applying step loadings to a mock-up concrete specimen with a real crack. In addition, the experimental results are compared with one of the widely accepted conventional subset size determination algorithms, i.e., SSSIG.

This paper is organized as follows. First, a subset-optimized DIC algorithm is developed for crack opening evaluation in Section 2. Then, the proposed algorithm is experimentally validated in Section 3. Finally, this paper is concluded with a brief discussion.

2. Subset-optimized DIC algorithm

Fig. 1 shows the overview of subset-optimized DIC algorithm. The reference and test images are acquired from ROI on the target surface using a digital camera. The reference and test images are respectively obtained under the two different conditions, i.e., without and with external loading. First, R number of reference images are acquired from the target surface at a certain time interval without loading. Subsequently, the test images are captured under step loading condition along the predefined step T. The subset size is then statistically optimized using the reference images. Next, minute deformation according to step loadings is analyzed using the reference and test images with the optimized subset. Once the DIC analysis images are obtained at each loading step, crack opening phenomenon can be precisely evaluated through the post-processing procedure. The details of each procedure are as follows.

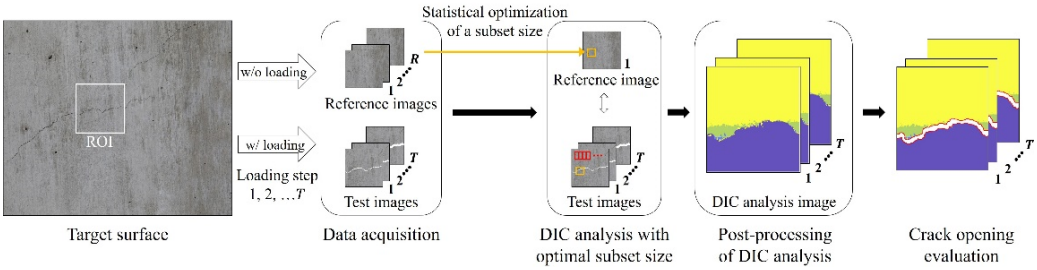

Fig. 1 Overview of the subset-optimized DIC algorithm for crack opening evaluation

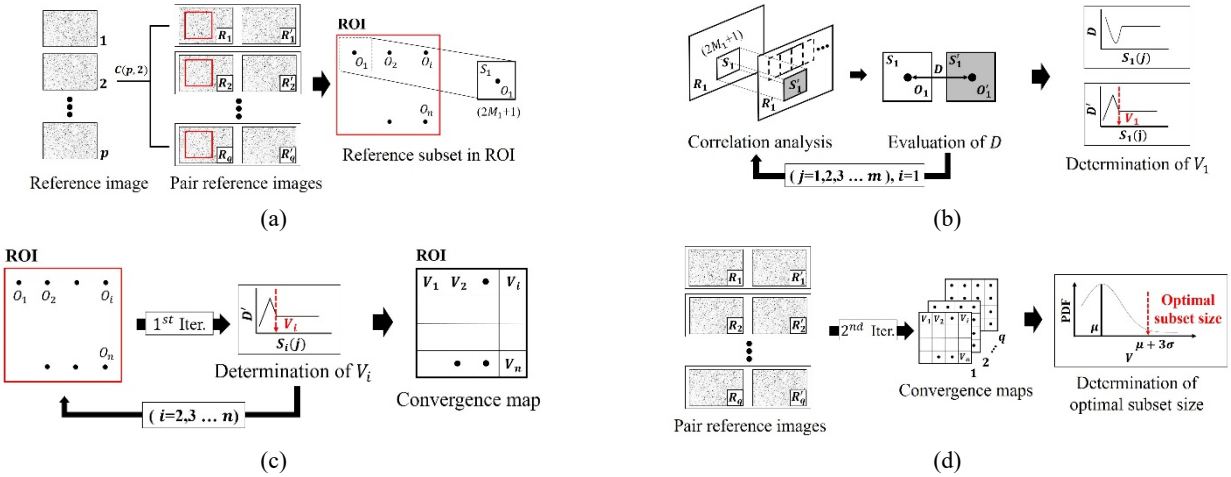

Fig. 2 Statistical optimization procedure of the subset size: (a) The initial setting of ROI and the reference subset; (b) The 1st iteration for evaluating the matching distance; (c) The 2nd iteration for establishing the convergence map; and (d) the 3rd iteration for determining the optimal subset size. R_q and R'_q are the pair of reference images. O_i is the seed point on R_q, and S_i is the reference subset centered at O_i. M_j is the size parameter of S_i, and S'_i is the matched subset of S_i centered at O'_i. D is the matching distance between S_i and S'_i. D' is the derivative of D, and $S_i(j)$ is $(2M_j + 1) \times (2M_j + 1)$. V_i is the converging size, and μ and σ are the average and standard deviation of the entire V_i

2.1 Statistical optimization of a subset size

Fig. 2 shows the statistical optimization procedure of the subset size. The proposed optimization procedure is composed of the following four steps: (a) the initial setting of ROI and the reference subset, (b) the 1st iteration for evaluating the matching distance, (c) the 2nd iteration for establishing the convergence map and (d) the 3rd iteration for determining the optimal subset size.

(a) The initial setting of ROI and the reference subset: First, p number of reference images are taken by the digital camera at a certain time interval without any deformation of the target structure, as shown in Fig. 2(a). The pairs of reference images, i.e., R_q and R'_q, are then selected via the two different combinations of reference images, which generate q pairs of reference images. Subsequently, ROI to be analyzed is selected within R_q, and the seed point O_i is then spatially assigned with a certain spatial interval on ROI. Note that the spatial interval of O_i should not be larger than the minimum size of the reference subset S_i to be investigated in the subsequent step. Once O_i is assigned on ROI, S_1 centered at O_1 starts to be determined with the size of $(2\,\mathrm{M}_1+1) \times (2\mathrm{M}_1+1)$ to have integer pixel values.

(b) The 1st iteration for evaluating the matching distance: NCC of S_1 with respect to R'_1 is calculated to establish the correlation coefficient (C_{NCC}) map as depicted in Fig. 2(b). C_{NCC} can be expressed by (Giachetti 2000)

$$
\begin{aligned}
C_{NCC} &= \sum_{a=-M_j}^{M_j}\sum_{b=-M_j}^{M_j}\left[\frac{[f(x_a,y_b)-f'][g(x'_a,y'_b)-g']}{\Delta f \Delta g}\right] \\
\Delta f &= \sqrt{\sum_{a=-M_j}^{M_j}\sum_{b=-M_j}^{M_j}[f(x_a,y_b)-f']^2}, \\
\Delta g &= \sqrt{\sum_{a=-M_j}^{M_j}\sum_{b=-M_j}^{M_j}[g(x'_a,y'_b)-g']^2}, \\
f' &= \frac{1}{(2M_j+1)^2}\sum_{a=-M_j}^{M_j}\sum_{b=-M_j}^{M_j} f(x_a,y_b), \\
g' &= \frac{1}{(2M_j+1)^2}\sum_{a=-M_j}^{M_j}\sum_{b=-M_j}^{M_j} g(x'_a,y'_b).
\end{aligned}
\tag{1}
$$

where f and g represent the grayscale intensity values at spatial points (x_a, y_b) and (x'_a, y'_b) in R_q and R'_q, respectively.

The pixel of the highest C_{NCC} within the C_{NCC} map is selected as O'_1, which is the center point of the matched subset S'_1. Physically, S'_1 is the most similar to S_1 within R'_1. S'_1 is then assigned to R_1 centered at O'_1. If there is no deformation between R_q and R'_q, O'_i and O_i theoretically have the same locations on R_q and R'_q, respectively. Next, the matching distance D between S_1 and S'_1 is computed using O_1 and O'_1, which is given by

$$
D = \sqrt{(x_i - x'_i)^2 + (y_i - y'_i)^2} \tag{2}
$$

where (x_i, y_i) and (x'_i, y'_i) are the spatial points of O_i and O'_i on R_q and R'_q, respectively.

Now, C_{NCC} is iteratively calculated by increasing $S_1(j)$, i.e., $(2M_j+1)$ x $(2M_j+1)$. Here, M_j (j = 1, 2, 3 … m) is the size parameter of S_i, and $S_i(j)$ should be smaller than ROI. Then, D can be obtained depending on $S_1(j)$. When $S_i(j)$ has a small value, D typically fluctuates as shown in Fig. 2(b), because the lack of the distinctive surface features within S_i makes it difficult to find the exact location of S'_i. On the other hand, D will converge after $S_i(j)$ exceeds a certain value, which physically implies that sufficient surface features are secured within the subset. The threshold value can be considered as the minimum converging size V_1, which is determined when the derivative of D (D') becomes 0, as shown in Fig. 2(b).

(c) The 2nd iteration for establishing the convergence map: As for O_i (i = 2, 3 … n), V_i can be obtained by repeating the 1st iteration as described in Fig. 2(c). Then, V_i is assigned to the corresponding O_i within ROI, which is called the convergence map when it comes to R_1 and R'_1. Physically, V_i in the convergence map means the minimum subset size required for proper DIC analysis with respect to each O_i within ROI.

(d) The 3rd iteration for determining the optimal subset size: q number of convergence maps can be obtained from R_q and R'_q, as shown in Fig. 2(d). The multiple convergence maps are used to minimize the random measurement noises which is caused during the image acquisition process. If the random measurement noises are more dominant than the surface features within a certain subset size, V_i will be increased. Thus, for each pair of reference images, V_i might be different depending on the random measurement noises, even at the same O_i. Finally, the optimal subset size is statistically determined by using the SD (σ) and mean (μ) with respect to V_i.

2.2 Post-processing for crack opening evaluation

Once the subset size is optimized, deformation of each subset within ROI can be computed between the reference and test images using the optimal subset size, as shown in Fig. 1. Although the DIC analysis images can be obtained from each loading step, precise crack opening evaluation is difficult due to undesired pixel-wise noise components. Thus, post-processing is necessary for removing the noise components.

Fig. 3 shows the overview of post-processing. It is assumed that the crack opens along the y direction within ROI in this study, but it can be easily extended to various directional cracks. First, the crack opening boundaries can be expressed by the magnitude of deformation gradients (G), which is given by

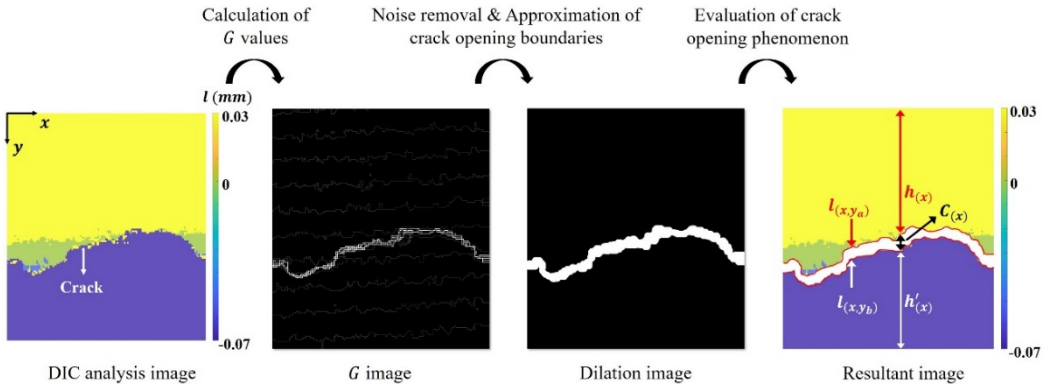

Fig. 3 Overview of post-processing for crack opening evaluation: G is the magnitude of the deformation gradient along the x and y directions. $l_{(x,y_a)}$ and $l_{(x,y_b)}$ are the deformations of the top and lowest pixels of the crack boundaries, $h_{(x)}$ and $h'_{(x)}$ are the mean deformations of top and bottom faces from $l_{(x,y_a)}$ and $l_{(x,y_b)}$. $C_{(x)}$ is the crack opening deformation calculated by the absolute difference between $h_{(x)}$ and $h'_{(x)}$

$$G = \sqrt{\left(\frac{\partial I}{\partial x}\right)^2 + \left(\frac{\partial I}{\partial y}\right)^2} \tag{3}$$

where $\frac{\partial I}{\partial x}$ and $\frac{\partial I}{\partial y}$ are the deformation gradients of the target image I along the x and y directions.

Once the G values are computed within the entire ROI, the G image can be obtained as shown in Fig. 3. Then, Otsu method is employed to remove the noises and to binarize the G image (Otsu 1979). Subsequently, the crack opening boundaries are approximated by a dilation method, resulting in the dilation image as shown in Fig. 3 (Maragos and Schafer 1987). Finally, the extracted crack opening boundaries are overlapped on the DIC analysis image, which is called the resultant image in Fig. 3. On the resultant image, crack opening deformation $C_{(x)}$ is calculated using the absolute difference between the mean deformation of top and bottom crack boundaries along the x direction, which is given by

$$\begin{aligned} C_{(x)} &= \left|h_{(x)} - h'_{(x)}\right| \\ h_{(x)} &= \frac{\sum_{\omega=1}^{a} l_{(x,y_\omega)}}{n_x}, \\ h'_{(x)} &= \frac{\sum_{\omega=b}^{c} l_{(x,y_\omega)}}{n'_x}. \end{aligned} \tag{4}$$

where $h_{(x)}$ and $h'_{(x)}$ are the mean deformations of top and bottom rows from the crack boundaries. $l_{(x,y_a)}$ and $l_{(x,y_b)}$ are the deformations of the top and lowest pixels of the crack boundaries, and $l_{(x,y_c)}$ is the deformation of the lowest pixel in the DIC analysis image. n_x and n'_x are the numbers of pixels from the first pixel to y_a and from y_b to y_c along the y direction, respectively.

3. Experimental validation

The proposed algorithm is experimentally validated using a mock-up concrete specimen and a pressure machine. To quantitatively evaluate the crack opening phenomenon, five step pressure loadings are used in the tests. The test results are then compared with SSSIG algorithm as well as the ground truth obtained by direct measurement.

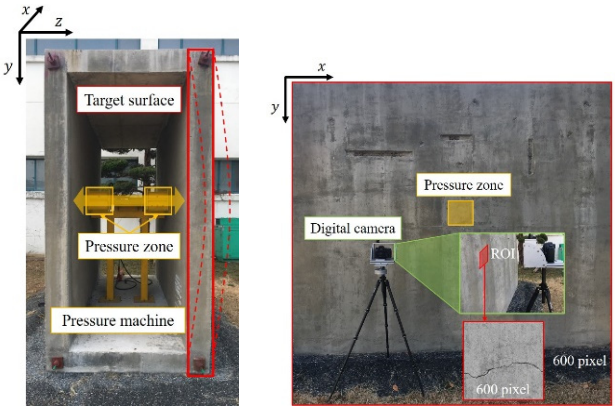

(a) (b)

Fig. 4 Experimental setup: (a) the side view of the mock-up concrete specimen; and (b) the front view with the data acquisition system

3.1 Experimental setup

Fig. 4 shows the experimental setup consisted of the digital camera, mock-up concrete specimen and pressure machine. The overall test procedures are as follows. First, 4 reference images are acquired using the digital camera without loading condition during 20 seconds. Then, the 5 step loadings are applied to the mock-up concrete specimen using the pressure machine, each loading step is controlled by the z directional displacements of 15 mm, 17.5 mm, 20 mm, 21 mm and 22 mm. Here, the specimen is bended because the pressure machine push out the specimen along the z direction as shown in Fig. 4(a). To investigate the crack opening, ROI containing one of the x directional surface cracks is intentionally selected and tested in this study. The selected crack gradually opens along the y direction as shown in Fig. 4(b).

The test images are captured outside the specimen along each loading step as displayed in Fig. 4(b). The size of ROI is 600 × 600 pixels (30 × 30 mm^2) on the target specimen. The digital camera is a Canon EOS 5D Mark 4 with a 100 mm F 2.8 L macro IS USM lens. The image resolution is 6720 × 4480 pixels when the working distance between the camera lens and the specimen surface is 475 mm. The pixel resolution is physically equivalent to 50 μm. The reference and test images are obtained under the outdoor condition, and the camera setting is fixed at ISO 1000, F 16 and an exposure time of 0.01 seconds.

3.2 Experimental results

The 6 pairs of the reference images are obtained from 4 reference images. Subsequently, 10,000 O_i values are assigned on ROI with respect to the spatial interval of 6 pixels. For all O_i, V_i values are determined while increasing M_j from 3 to 27 with an interval of 1. Finally, 6 convergence maps are established from the 6 pairs of reference images. The resultant optimal subset size can be statistically determined by summing the σ and μ values with respect to 60,000 V_i values.

Fig. 5 shows the distribution of V_i according to subset length, which is fitted by a Frechet distribution. The V_i value varies from the minimum of 7 × 7 pixels to the maximum of 53 × 53 pixels. Here, 85 % of V_i has the subset sizes between 7 × 7 pixels and 13 × 13 pixels, as shown in Fig. 5. Then, the rest 15 % of V_i has relatively large subset sizes over 15 × 15 pixels because the corresponding areas to the rest 15 % have insufficient features compared to other ordinary areas. The computed the σ and μ values with respect to the entire V_i value are 8.7 and 2.2, respectively. Based on the statistical analysis with a confidence interval of 99 %, the optimal subset size is determined as 17 × 17 pixels.

Next, the representative test results obtained using the optimal subset size at the loading step 5 are shown in Fig. 6. Fig. 6(a) shows the DIC analysis image with the optimal subset size of 17 × 17 pixels. Once the G values are calculated using Eq. (3), the G image, which successfully shows the crack boundaries, can be obtained as depicted in Fig. 6(b). Then, Fig. 6(c) shows the corresponding dilation image, and the representative crack opening deformation at $C_{(300)}$ is shown in Fig. 6(d).

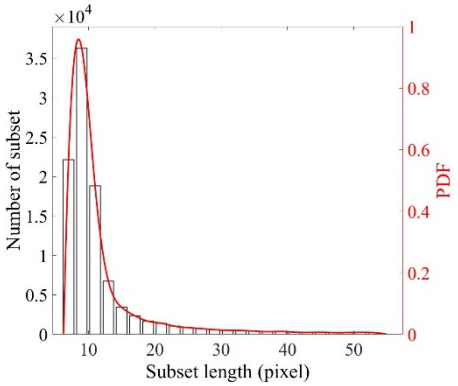

Fig. 5 Distribution of V_i according to the subset length

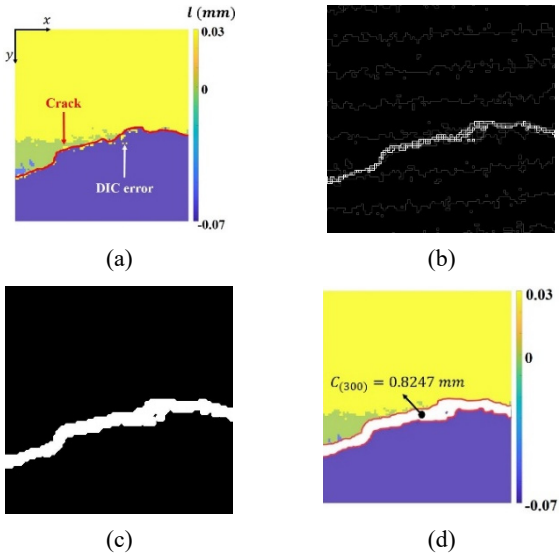

Fig. 6 The representative test results at the loading step 5: (a) DIC analysis image, (b) G image, (c) dilation image and (d) resultant image: l is the deformation of the target surface and $C_{(300)}$ is the crack opening deformation at x of 300th pixels

In order to examine the superiority of the proposed algorithm, the comparative study is conducted on the same test data using SSSIG (Pan *et al*. 2008). According to the typical procedure of SSSIG, the two seed points are randomly selected within ROI, as shown in Fig. 7(a). To equivalently compare the test results, the seed points are intentionally selected among O_i. Then, the SD error values, i.e., $SDerror(x)$ and $SDerror(y)$, are calculated by

$$SDerror(x) = \left[\frac{N(\eta)}{\sum\sum(f_x)^2}\right]^{\frac{1}{2}},$$
$$SDerror(y) = \left[\frac{N(\eta)}{\sum\sum(f_y)^2}\right]^{\frac{1}{2}}. \quad (5)$$

where $N(\eta)$ is the noise variance calculated using the two images acquired with 5 second time interval. $\sum\sum(f_x)^2$ and $\sum\sum(f_y)^2$ are the SSSIG values along the x and y axes. f_x and f_y are the first-order derivatives of grayscale intensities within the subset *a*long the x and y directions, respectively. The threshold of the $SDerror(x)$ and $SDerror(y)$ is set to 0.005, which is recommended by Pan *et al*. (2008). The subset size is similarly increased from 7 × 7 pixels to 55 × 55 pixels, which is equivalent to the proposed algorithm.

Figs. 7(b) and (c) show the subset size determination results obtained by SSSIG. The subset sizes of 33 × 33 and 43 × 43 pixels are differently determined depending on the seed point location by employing the threshold value of 0.005. It is importantly noted that these two different subset size results are obtained from the two different locations which are randomly selected.

Fig. 8 compares tests results obtained using the proposed and SSSIG algorithms. According to the loading

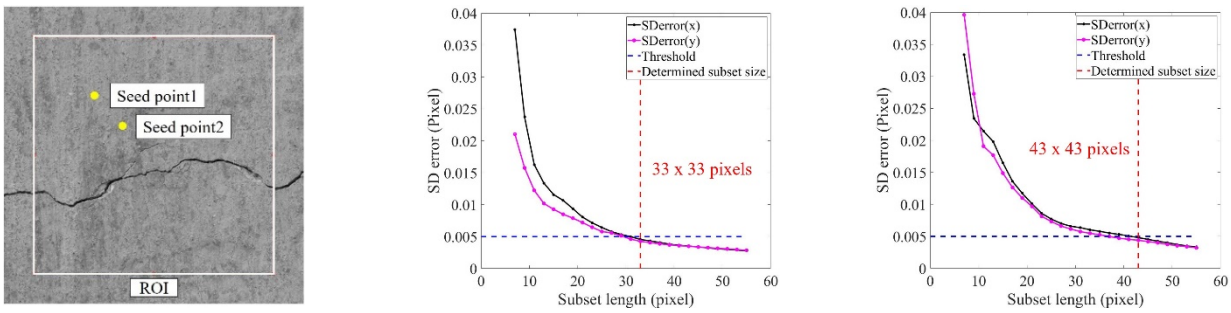

(a) (b) (c)

Fig. 7 Determination of subset sizes using SSSIG at the two randomly selected seed points: (a) location of two seed points on ROI; (b) subset size determination result at seed point 1 and (c) subset size determination result at seed point 2

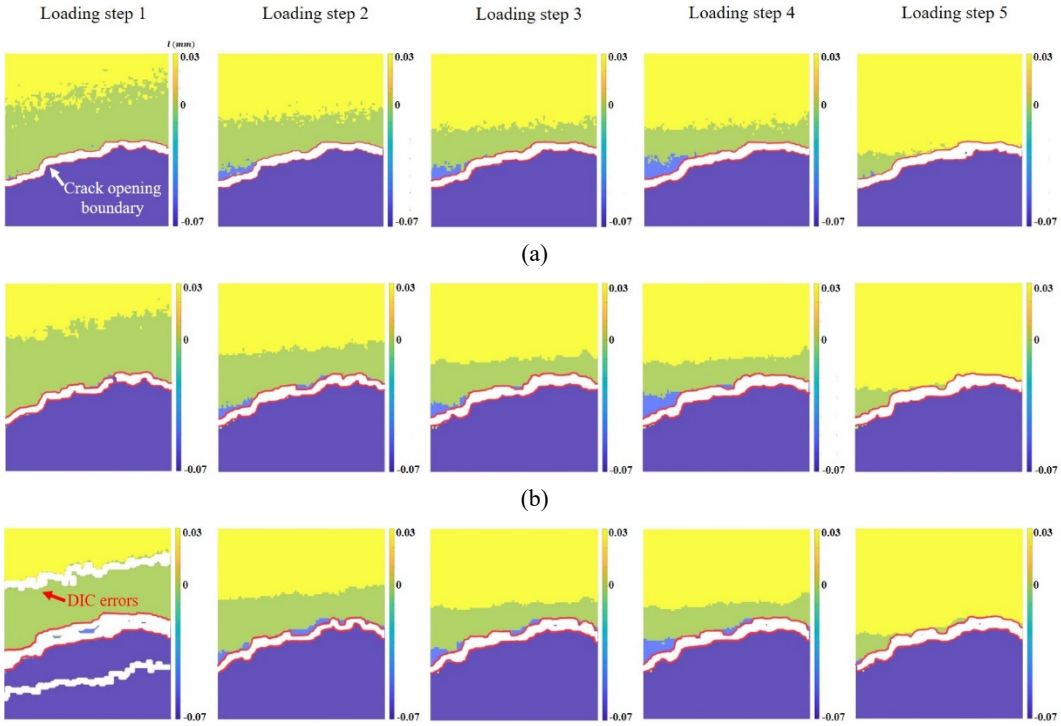

(a)

(b)

(c)

Fig. 8 DIC test results according to the loading steps: (a) the proposed algorithm (17 × 17 pixels); (b) SSSIG (33 × 33 pixels); and (c) SSSIG (43 × 43 pixels)

steps, the proposed algorithm shows that the crack boundaries are gradually opened as displayed in Fig. 8(a). Similarly, the SSSIG case (33 × 33 pixels) well traces the crack opening phenomenon as shown in Fig. 8(b). However, the SSSIG case (43 × 43 pixels) produces severe DIC errors especially at the loading step 1 as shown in Fig. 8(c). Moreover, the crack boundaries are overestimated compared to the first two cases, meaning that the subset size significantly affect to the DIC accuracy. In particular, the SSSIG cases shows the different DIC accuracy depending on the seed point selection, while the proposed algorithm shows stable performance, as shown in Fig. 8.

To quantitatively compare the test results of the three cases, μ and σ with respect to difference of all $C_{(x)}$ values between each loading step are calculated. Here, μ physically means whether the crack opening is accurately evaluated, and σ shows the spatial consistency of crack opening phenomenon.

Fig. 9 shows the comparison results between the ground truth with the proposed and SSSIG algorithms. Fig. 9(a) shows that the proposed algorithm is good agreement with the ground truth represented by the solid line. The errors of μ compared with the ground truth are 1.5, 0.8, 0.1 and 3.6 μm at each loading step. As expected, the SSSIG case (33 × 33 pixels) also shows the acceptable errors of 1.4, 3.7, 4.6 and 0.5 μm as displayed in Fig. 9(b). As for σ, the proposed algorithm shows 4.9, 4.5, 4.7 and 5.9 μm, and the SSSIG case (33 × 33 pixels) produces 4.9, 4.4, 3.8 and 3.9 μm. These σ values means that the above two cases consistently trace the crack opening phenomenon along the entire crack. On the other hand, the SSSIG case (43 × 43 pixels) reveals the μ errors of 62.7, 5.4, 5 and 1.7 μm and

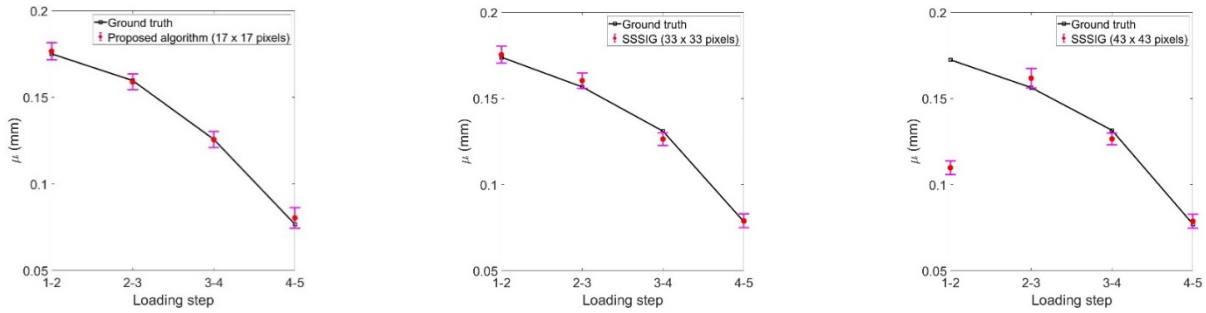

(a) (b) (c)

Fig. 9 The comparison results between the ground truth with (a) the proposed algorithm (17 × 17 pixels); (b) SSSIG (33 × 33 pixels); and (c) SSSIG (43 × 43 pixels)

the σ values of 4, 5.6, 3.4 and 4 μm, respectively, as shown in Fig. 9(c). In particular, the severe error of 62.7 μm occurs at the first loading step, because the subset size of 43 × 43 pixels is too large to precisely trace the minute deformation of the target surface. It is interesting thing to observe is that Figs. 9(b) and (c) show completely different results even though the results are obtained from SSSIG, meaning that the SSSIG results highly depend on experts' subjective judgement. In this perspective, the proposed algorithm has superiority compared to SSSIG.

4. Conclusions

This paper proposed a digital image correlation (DIC) analysis algorithm with novel statistical optimization of a subset size for crack opening phenomenon evaluation. The effectiveness of the proposed algorithm was experimentally demonstrated using a mock-up concrete specimen with a real crack and pressure machine. Then, the test results were compared with one of the widely accepted subset size determination algorithms, i.e., sum of square of subset intensity gradient (SSSIG). The validation test results revealed that the optimal subset size of 17 × 17 pixels, which was statistically determined by the proposed algorithm without experts' subjective intervention, well traced the crack opening phenomenon. On the other hand, the SSSIG results showed that spatially different severe DIC errors could be produced depending on user's judgement.

In order to apply the proposed algorithm to in-situ structures, several data acquisition requirements such as sufficient surface features, constant camera pose and lighting conditions should be satisfied. In this perspective, further studies are still necessary for overcoming the aforementioned technical limitations. For example, the aging concrete structure surface, which was shown in this study, has enough distinctive surface features without any surface treatment. On the other hand, homogeneous and clean materials such as pure metals or glasses may need to add irregular speckle patterns on the target surface for applying the proposed algorithm. As the follow-up study, a camera pose-free and laser-generated speckle pattern DIC techniques with the optimal subset size are now being developed. Furthermore, the proposed technique will be applied to full-field and real-time deformation measurement for in-situ structures.

Acknowledgments

This work was supported by the National Research Foundation of Korea (NRF) grant funded by the Korea government (MSIT) (2018R1A1A1A05078493).

References

An, Y.K. and Sohn, H. (2015), "Visualization of non-propagating lamb wave modes for fatigue crack evaluation", *J. Appl. Phys.*, **117**, 114904. https://doi.org/10.1063/1.4906499

An, Y.K., Park, B. and Sohn, H. (2013), "Complete noncontact laser ultrasonic imaging for automated crack visualization in a plate", *Smart Mater. Struct.*, **22**(2), 025022. https://doi.org/10.1088/0964-1726/22/2/025022

An, Y.K., Yang, J., Hwang, S. and Sohn, H. (2015), "Line laser lock-in thermography for instantaneous imaging of cracks in semiconductor chips", *Opt. Lasers Eng.*, **73**, 128-136. https://doi.org/10.1016/j.optlaseng.2015.04.013

Bohacova, M. (2013), "Methodology of short fatigue crack detection by the eddy current method in a multi-layered metal aircraft structure", *Eng. Fail. Anal.*, **35**(15), 597-608. https://doi.org/10.1016/j.engfailanal.2013.06.009

Caizzone, S. and DiGiampaolo, E. (2015), "Wireless passive RFID crack width sensor for structural health monitoring", *IEEE Sens J.*, **15**(12), 6767-6774. https://doi.org/10.1109/JSEN.2015.2457455

Camerini, C., Rebello, J.M.A., Braga, L., Santos, R., Chady, T., Psuj, G. and Pereira, G. (2018), "In-line inspection tool with eddy current instrumentation for fatigue crack detection", *Sensors*, **18**(7), 2161. https://doi.org/10.3390/s18072161

Destrebecq, J.F., Toussaint, E. and Ferrier, E. (2011), "Analysis of cracks and deformations in a full scale reinforced concrete beam using a digital image correlation technique", *Experim. Mech.*, **51**(6), 879-890. https://doi.org/10.1007/s11340-010-9384-9

Ghorbani, R., Matta, F. and Sutton, M.A. (2014), "Full-field deformation measurement and crack mapping on confined masonry walls using digital image correlation", *Experim. Mech.*, **55**(1), 227-243. https://doi.org/10.1007/s11340-014-9906-y

Giachetti, A. (2000), "Matching techniques to compute image motion", *Image Vis Comput.*, **18**(3), 247-260. https://doi.org/10.1016/S0262-8856(99)00018-9

Hua, T., Xie, H., Wang, S., Hu, Z., Chen, P. and Zhang, Q. (2011),

"Evaluation of the quality of a speckle pattern in the digital image correlation method by mean subset fluctuation", *Opt. Laser Technol.*, **43**(1), 9-13. https://doi.org/10.1016/j.optlastec.2010.04.010

Hutt, T. and Cawley, P. (2009), "Feasibility of digital image correlation for detection of cracks at fastener holes", *NDT & E Int.*, **42**(2), 141-149. https://doi.org/10.1016/j.ndteint.2008.10.008

Jang, K. and An, Y.K. (2018), "Multiple crack evaluation on concrete using a line laser thermography scanning system", *Smart Struct. Syst., Int. J.*, **22**(2), 201-207. https://doi.org/10.12989/sss.2018.22.2.201

Kim, N., Jang, K. and An, Y.K. (2018), "Self-sensing nonlinear ultrasonic fatigue crack detection under temperature variation", *Sensors*, **18**(8), 2527. https://doi.org/10.3390/s18082527

Lecompte, D., Smits, A., Bossuyt, S., Sol, H., Vantomme, J., Van Hemelrijck, D. and Habraken, A.M. (2006), "Quality assessment of speckle patterns for digital image correlation", *Opt. Laser Eng.*, **44**(11), 1132-1145. https://doi.org/10.1016/j.optlaseng.2005.10.004

Li, T., Almond, D.P. and Rees, D.A.S. (2011), "Crack imaging by scanning pulsed laser spot thermography", *NDT & E Int.*, **44**(2), 216-225. https://doi.org/10.1016/j.ndteint.2010.08.006

Maragos, P. and Schafer, R. (1987), "Morphological filters-part I: their set-theoretic analysis and relations to linear shift-invariant filters", *IEEE Trans. Signal Process.*, **35**(8), 1153-1169. https://doi.org/10.1109/TASSP.1987.1165259

Marindra, A.M.J. and Tian, G.Y. (2018), "Chipless RFID sensor tag for metal crack detection and characterization", *IEEE T Microw Theory*, **66**(5), 2452-2462. https://doi.org/10.1109/TMTT.2017.2786696

Meng, L., Jin, G. and Yao, X. (2006), "Errors caused by misalignment of the optical camera axis and the object surface in the DSCM", *J. Tsinghua Univ.*, **46**, 1930-1932.

Otsu, N. (1979), "A threshold selection method from gray level histograms", *IEEE T. Syst. Man. Cybernet.*, **9**(1), 62-66.

Pan, B., Xie, H., Wang, Z., Qian, K. and Wang, Z. (2008), "Study on subset size selection in digital image correlation for speckle patterns", *Opt. Express*, **16**(10), 7037-7048. https://doi.org/10.1364/OE.16.007037

Pour-Ghaz, M., Barrett, T., Ley, T., Materer, N., Apblett, A. and Weiss, J. (2014), "Wireless crack detection in concrete elements using conductive surface sensors and radio frequency identification technology", *J. Mater. Civil Eng.*, **26**(5), 923-929. https://doi.org/10.1061/(ASCE)MT.1943-5533.0000891

Qaddoumi, N., Ranu, E., McColskey, J.D., Mirshahi, R. and Zoughi, R. (2000), "Microwave detection of stress-induced fatigue cracks in steel and potential for crack opening determination", *Res. Nondestruct. Eval.*, **12**(2), 87-103. https://doi.org/10.1080/09349840009409652

Schreier, H.W. and Sutton, M.A. (2002), "Systematic errors in digital image correlation due to undermatched subset shape functions", *Experim. Mech.*, **42**, 303-310. https://doi.org/10.1007/BF02410987

Yaofeng, Y.F. and Pang, H.J. (2007), "Study of optimal subset size in digital image correlation of speckle pattern images", *Opt. Lasers Eng.*, **45**, 967-974. https://doi.org/10.1016/j.optlaseng.2007.01.012

Sutton, M.A., McNeill, S.R., Jang, J. and Babai, M. (1988), "Effects of subpixel image restoration on digital correlation error estimates", *Opt. Eng.*, **27**, 870-877. https://doi.org/10.1117/12.7976778

Tong, W. (2005), "An evaluation of digital image correlation criteria for strain mapping applications", *Strain*, **41**(4), 167-175. https://doi.org/10.1111/j.1475-1305.2005.00227.x

Tsukamoto, A., Hato, T., Adachi, S., Oshikubo, Y., Tsukada, K. and Tanabe, K. (2018), "Development of eddy current testing system using HTS-SQUID on a hand cart for detection of fatigue cracks of steel plate used in expressways", *IEEE T. Appl. Superconduct.*, **28**(4), 1-5. https://doi.org/10.1109/TASC.2018.2795614

Wang, Z.Y., Li, H.Q., Tong, J.W. and Ruan, J.T. (2007), "Statistical analysis of the effect of intensity pattern noise on the displacement measurement precision of digital image correlation using self-correlated images", *Expim. Mech.*, **47**(5), 701-707. https://doi.org/10.1007/s11340-006-9005-9

Yaofeng, S. and Pang, J.H.L. (2007), "Study of optimal subset size in digital image correlation of speckle pattern images", *Opt. Laser Eng.*, **45**(9), 967-974. https://doi.org/10.1016/j.optlaseng.2007.01.012

Yun, T. and Lim, S. (2014), "High-Q and miniaturized complementary split ring resonator-loaded substrate integrated waveguide microwave sensor for crack detection in metallic materials", *Sensor Actuat. A-Phys.*, **214**, 25-30. https://doi.org/10.1016/j.sna.2014.04.006

HJ